communications materials

ARTICLE

https://doi.org/10.1038/s43246-022-00224-8 OPEN

Coexisting Z-type charge and bond order in metallic $NaRu_2O_4$

Arvind Kumar Yogi[1,2,3,11]✉, Alexander Yaresko[4,11], C. I. Sathish[1,2], Hasung Sim[1,2], Daisuke Morikawa[5], Juergen Nuss[4], Kenji Tsuda[6], Yukio. Noda[5,7], Daniel I. Khomskii[8] & Je-Geun Park[1,2,9,10]✉

How particular bonds form in quantum materials has been a long-standing puzzle. Two key concepts dealing with charge degrees of freedom are dimerization (forming metal-metal bonds) and charge ordering. Since the 1930s, these two concepts have been frequently invoked to explain numerous exciting quantum materials, typically insulators. Here we report dimerization and charge ordering within the dimers coexisting in metallic $NaRu_2O_4$. By combining high-resolution x-ray diffraction studies and theoretical calculations, we demonstrate that this unique phenomenon occurs through a new type of bonding, which we call Z-type ordering. The low-temperature superstructure has strong dimerization in legs of zigzag ladders, with short dimers in legs connected by short zigzag bonds, forming Z-shape clusters: simultaneously, site-centered charge ordering also appears. Our results demonstrate the yet unknown flexibility of quantum materials with the intricate interplay among orbital, charge, and lattice degrees of freedom.

[1] Center for Correlated Electron Systems, Institute for Basic Science (IBS), Seoul 08826, Korea. [2] Department of Physics and Astronomy, Seoul National University, Seoul 08826, Korea. [3] UGC-DAE Consortium for Scientific Research, Indore 452001, India. [4] Max-Planck-Institut für Festkörperforschung, 70569 Stuttgart, Germany. [5] Institute of Multidisciplinary Research for Advanced Materials, Tohoku University, Sendai 980-8577, Japan. [6] Frontier Research Institute for Interdisciplinary Sciences, Tohoku University, Sendai 980-8577, Japan. [7] J-PARC Center, Japan Atomic Energy Agency, 2-4 Shirakata, Tokai, Ibaraki 319-1195, Japan. [8] Institute of Physics II, University of Cologne, 50937 Cologne, Germany. [9] Center for Quantum Materials, Seoul National University, Seoul 08826, Korea. [10] Institute of Applied Physics, Seoul National University, Seoul 08826, Korea. [11] These authors contributed equally: Arvind Kumar Yogi, Alexander Yaresko. ✉email: yogi.arvind2003@gmail.com; jgpark10@snu.ac.kr

Chemical bonding lies at the heart of all-natural sciences like condensed matter physics, chemistry, and even biology. As such, the understanding of chemical bonding was a great puzzle for a long time. In the long and rich history of condensed matter physics, one cannot emphasize strongly enough the importance of the two basic concepts: dimerization[1] and charge ordering[2], both born in the 1930s. However, these two phenomena have been rarely found to coexist in one compound, much less in metallic systems.

Many studies in the late 1990s and early 2000s demonstrated, one example after another, how the new patterns emerge out of simple structures: hexamers in $ZnCr_2O_4$[3], octamers in $CuIr_2S_4$[4], spontaneous dimensionality reduction in $Tl_2Ru_2O_7$[5], and the formation of trimeron in Fe_3O_4[6], to name only a few. Despite the various properties, an ever occurring theme is that these phenomena typically happen near the metal–insulator boundary, with the ordered states usually insulating. This characteristic feature is naturally captured by Mott–Hubbard physics[7], and it is particularly prominent among frustrated magnets[8–11]. It is relatively less well-known how this rich physics plays out in metallic systems; it remains unchartered territory to date. One can imagine that this question may become more important in the newly emerging field of quantum materials that increasingly include metallic systems[12].

Ru has a special place in this extensive search because of its two characteristic features: the modest spin–orbit coupling (SOC), not too small nor too large compared to the Coulomb energy and the bandwidth; another is relatively stronger importance of orbital physics[7]. This combination of the two has been behind the active researches on Ru oxides; for instance, superconducting Sr_2RuO_4 and ferromagnetic $SrRuO_3$ are two prominent examples[13,14]. In comparison, there have been few studies on Na–Ru–O systems, including $NaRu_2O_4$. Using neutron diffraction, the authors of ref. [15] determined that its room-temperature structure has the space group of *Pnma*, the typical orthorhombic structure among oxides: to our best knowledge, it was initially reported in 1975[16] before being re-examined in 2006. It was reported to have a paramagnetic susceptibility down to the lowest temperature. While studying another Na compound, $Na_{2.7}Ru_4O_9$[17] which was also investigated in the same ref. [15], we realized that the high-temperature phase of these Na–Ru–O systems could exhibit exciting new unreported properties and hence deserve careful studies.

In this report, we made extensive studies of both structure and physical properties of $NaRu_2O_4$ over a wide temperature range up to 600 K above which it becomes chemically unstable. We made the high-resolution XRD study above room temperature to find a surprising first-order phase transition during this study. We found that $NaRu_2O_4$ undergoes a metal–metal phase transition below 535 K with a distinct structure change, from a $CaFe_2O_4$-type structure with the orthorhombic *Pnma* symmetry at a higher temperature to a monoclinic structure $P112_1/a$ below T_c. By combining experimental and theoretical studies, we found that at this transition we have simultaneously a site-centered charge ordering coexisting with dimerization.

Results and discussion

Bulk properties. Electrical resistivity (ρ) measurements were carried out using a homemade system equipped with a furnace (300–685 K) and a pulsed-tube cryostat with the base temperature of 3 K. The electrical resistance was measured in a four-point geometry, where contacts were made using silver paint and 25 μm gold wire as shown in the inset of Fig. 1a. The current was applied perpendicular to the single crystal length, which is the crystallographic *b*-axis. As the single crystals are all in a thin needle form, we could not measure the resistivity along with the other crystallographic directions. We tested several long rod-shaped as-grown crystals and discovered the same transition (see also Supplementary Fig. 1). The resistivity data shows that a phase transition occurs in $NaRu_2O_4$ at $T_c = 535$ K with small hysteresis in the electrical resistivity, a sign of a weak first-order phase transition at T_c. We will extensively discuss this transition below; it is the main feature of $NaRu_2O_4$.

The resistivity $\rho(T)$ data measured down to 3.3 K indicates metallic behavior with a room temperature resistivity of ~40 μΩ cm. To have a quantitative understanding, we analyzed the results theoretically using the Bloch–Grüneisen model. The following formula gives the expression for the temperature-dependent part of the metallic resistivity:

$$\rho \approx \left(\frac{3}{\hbar e^2 v_F^2}\right)\frac{k_B T}{M v_s^2}\int |v(q)|^2\left[\frac{(\hbar\omega/k_B T)^2 q^3 dq}{(\exp(\hbar\omega/k_B T)-1)(1-\exp(-\hbar\omega/k_B T))}\right], \quad (1)$$

where $v(q)$ is the Fourier transform of the potential associated with one lattice site and v_s is the sound velocity. When Eq. (1) was considered for the acoustic phonon contribution, it leads to the Bloch–Grüneisen function as shown below:

$$\rho_{e-ph}(T,\theta_D) = 4A_{ac}(T/\theta_D)^4 \times T\int_0^{\theta_D/T} x^5(e^x-1)^{-1}(1-e^{-x})^{-1}dx, \quad (2)$$

where $x = \hbar\omega/k_B T$, θ_D is Debye temperature, and A_{ac} is a proportionality constant. The total resistivity of a material can be written as

$$\rho(T) = \rho_0 + \rho_{e-ph}(T,\theta_D),$$

where ρ_0 is the temperature-independent residual resistivity and the second term represents the electron–phonon scattering. The Bloch–Grüneisen model is found to work well for our study, and the theoretically estimated ρ is quite consistent with the experimental data for $NaRu_2O_4$. The characteristic Debye temperature (θ_ρ) and residual resistivity (ρ_0) is found to be 452.2 K and 35.9 μΩ cm, respectively.

We also measured magnetic susceptibility and specific heat of $NaRu_2O_4$ in the accessible temperature range of 2–300 K. The susceptibility (χ) for $NaRu_2O_4$ was measured in the temperature range between $1.9 \le T \le 300$ K with a 0.5 T of the external field applied perpendicular to the length of the as-grown crystal as in Fig. 1b. No magnetic ordering was observed in the measured temperature range. It is noticeable that the susceptibility is almost temperature-independent over the wide temperature range, showing a sizeable paramagnetic behavior consistent with the reported susceptibility data on the polycrystalline sample[15]. The low-temperature upturn is apparently due to some magnetic impurities, and it can be explained by using a modified Curie–Weiss formula as discussed in Supplementary Note 2 (see the red line in Fig. 1b). The fit yields the following values: Curie–Weiss temperature $\theta_{CW} = -1.8$ K, observed moment $\mu_{eff} = 0.04\,\mu_B$ per Ru atoms and $\chi_0 = 1.15 \times 10^{-7}$ $(cm^3/Ru\ mol)^{-1}$, where the latter is the temperature-independent van Vleck contribution to the susceptibility. The Curie–Weiss fit gives a significantly smaller observed moment, indicating negligible localized magnetic moments in $NaRu_2O_4$, similar to the reported polycrystalline sample[15].

The heat capacity was measured between $1.9 \le T \le 300$ K and is displayed in Fig. 1c. The heat capacity did not show any λ-type anomaly over the entire temperature range, confirming no long-range magnetic order from 300 to 1.9 K. Low-temperature heat capacity data were analyzed using the usual formula of $C_p = \gamma T + \beta T^3$, where γ is the electronic specific-heat coefficient and β is the phonon contribution at low temperature (see the

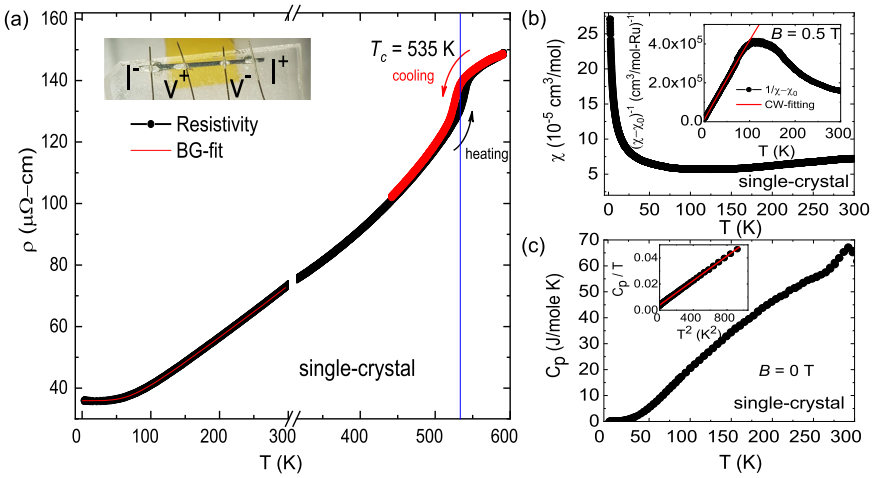

Fig. 1 Bulk properties. a The electrical resistivity data as a function of temperature is taken over single-crystal with the solid red line for the Bloch–Grüneisen model. Inset shows the single crystal used for the four-probe resistivity measurements. **b** Magnetic susceptibility (χ) measured at an applied magnetic field $B = 0.5$ T. The inset shows inverse susceptibility with the modified Curie–Weiss law (solid red line). **c** Temperature dependence of the specific heat C_p measured at zero fields ($B = 0$ T). Solid black circles are the raw data with C_p/T shown in the inset of the figure while solid red line is the corresponding $C_p/T = \gamma + \beta T^2$ fitting.

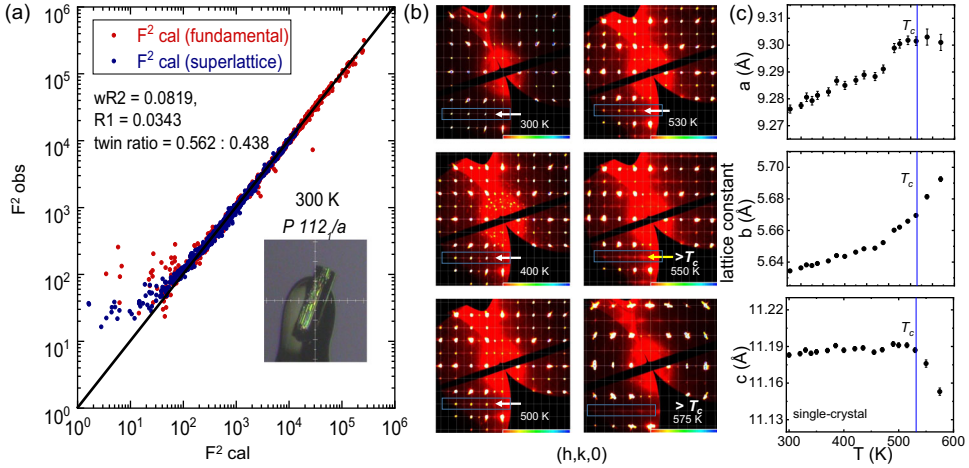

Fig. 2 Room-temperature SC-XRD refinement for LT-phase: Single-crystal XRD reciprocal-lattice images and lattice parameters across the structural transition. a The SC-XRD refinement includes a modified structural model with a new space group ($P112_1/a$) determined from CBED experiments. The refinement is performed by including a monoclinic merohedral twin model under twin law as (-100) (010) (00-1). The solid red and blue circles are fundamental and superlattice reflections, respectively. The inset of the figure shows the optical image of the measured crystal. **b** Single-crystal x-ray diffraction data measured at various temperatures below and above the phase transition ($T_c = 535$ K) for $NaRu_2O_4$. **c** The cell parameters with error bars of $NaRu_2O_4$ at different temperatures extracted from single-crystal XRD data. The vertical line corresponds to T_c.

inset of Fig. 1c). The electronic contribution to the specific heat (γ) for $NaRu_2O_4$ was 3.93 mJ/mol K^2, consistent with the metallic behavior.

Single-crystal XRD data and crystal structures at high and low temperatures. To understand the high-temperature phase transition seen in the resistivity data, we conducted high-resolution single-crystal diffraction experiments to obtain the most informative data. We performed the temperature-dependent SC-XRD experiment from 300 to 575 K using a single crystal diffractometer (XtaLAB P200, Rigaku) (see Fig. 2). In our room-temperature data, we observed $\mathbf{q} = (0, ½, 0)$ superlattice peak (satellite reflections). It is important to note that this presence of the satellite reflection cannot possibly be explained by the *Pnma* space group proposed in ref. [15].

While searching battling for a possible true structure at room temperature, we decided to employ the convergence beam electron diffraction (CBED) as it is the most powerful technique in determining the space group and gives crucial information about the lattice's symmetry[18] (see Fig. 3). The weak superlattice reflections in the x-ray diffraction experiments already form strong evidence for broken symmetry (both translation and rotational) and lattice distortion in a crystal. In addition, the superlattice peak at $\mathbf{q} = (0, ½, 0)$ disappears upon heating just above T_c. We collected CBED diffraction patterns along the various [100], [130], [001], and [201] axes as shown in Fig. 3a–c at room temperature. The CBED experiment revealed $P112_1/a$ symmetry (no. 14 with setting unique axis c[19]) at room temperature, a subgroup of the reported *Pnma* symmetry. Therefore, a modified structure model under group–subgroup relation is used to solve the room temperature SC-XRD data. We used the Shelx software[20] to address the twin problem in our refinement. In the twin refinement for $NaRu_2O_4$ SC-XRD data, we used a monoclinic merohedral twin model under twin law as

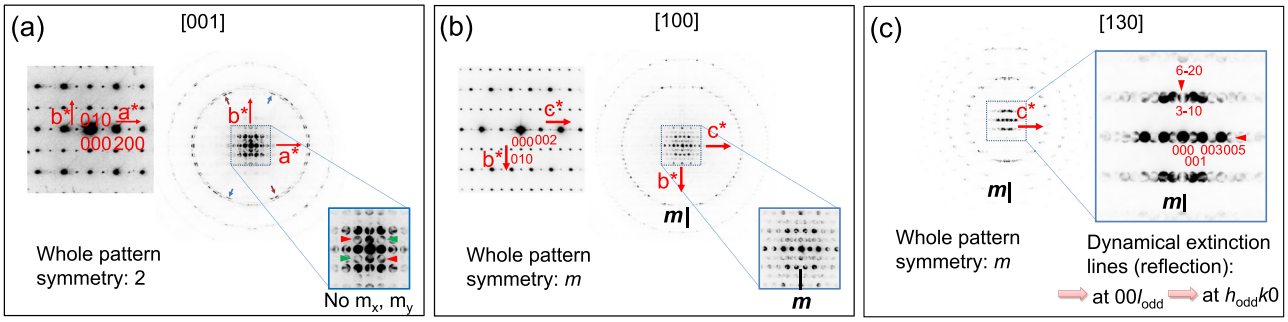

Fig. 3 The converge beam electron diffraction (CBED) patterns at room temperature in $NaRu_2O_4$ crystal. The CBED patterns are taken with (**a**) [001], (**b**) [100], and (**c**) [130] incidences. Whole pattern symmetries of the CBED patterns are two-fold symmetry for [001] incidence, mirror symmetry perpendicular to the c-axis for [100] and [130] incidences. Dynamical extinction lines were observed at 0 0 l_{odd} and h_{odd} k 0 reflections at [130] incidence.

Table 1 The single-crystal x-ray diffraction measurement of $NaRu_2O_4$ at 300 K is used for the refinement.

Atoms	x	y	z	U_{iso}	Site
Ru1(A)	0.05988(6)	0.10622(13)	0.11842(5)	0.0043(2)	4e
Ru1(B)	0.05614(7)	0.64469(14)	0.11228(4)	0.0042(2)	4e
Ru2(B)	0.08283(7)	0.14396(14)	0.60006(5)	0.0040(2)	4e
Ru2(A)	0.08712(7)	0.60733(14)	0.60517(4)	0.0042(2)	4e
Na1(A)	0.2383(3)	0.1310(9)	0.3396(2)	0.0160(6)	4e
Na1(B)	0.2412(3)	0.6313(9)	0.3417(3)	0.0208(7)	4e
O1A	0.2874(5)	0.1328(12)	0.6631(4)	0.0062(9)	4e
O1B	0.3030(5)	0.6215(13)	0.6541(4)	0.0066(9)	4e
O2A	0.3870(5)	0.1250(12)	0.9847(4)	0.0073(9)	4e
O2B	0.3829(5)	0.6171(12)	0.9676(4)	0.0065(9)	4e
O3A	0.4676(5)	0.1135(12)	0.2149(4)	0.0061(9)	4e
O3B	0.4783(5)	0.6232(11)	0.2240(4)	0.0067(9)	4e
O4A	0.0951(5)	0.1221(12)	0.9385(4)	0.0052(9)	4e
O4B	0.0775(5)	0.6322(11)	0.9310(4)	0.0065(9)	4e

The experimental structural result at room temperature has been determined by twin analysis (with twin (0.43748)) using the Shelx program[20]. The $P112_1/a$ symmetry is used for the refinement as obtained from CBED experiments. The reliable parameters of refinement are found to be: $wR2 = 0.0821$, $R1 = 0.0344$, GoF = $S = 1.162$: $a = 99.256(1)$ Å, $b = 5.634(1)$ Å, and $c = 11.154(1)$ Å; $\gamma = 90.10$ (1)°; volume = 581.7(1) Å^3. All the atoms in $NaRu_2O_4$ crystal-lattice are at 4e sites.

(-100) (010) (00-1) to get better refinement parameters and statistics as well. Supplementary Note 3 provides details of monoclinic merohedral twin model under twin law. All the reflection patterns collected at 300 K could be indexed as monoclinic $P112_1/a$ symmetry with a primitive lattice of $a = 9.273$ (6) Å, $b = 5.643$ (3) Å, and $c = 11.17$ (7) Å.

Table 1 summarizes the SC-XRD refinement results for the low-temperature (LT) phase (300 K). All the crystallographic sites were considered to be fully occupied and were kept fixed during the refinement. We carried out the structure analysis by including the twin structure of monoclinic cells. The structural parameters were finally determined from the least-squares refinement of the single-crystal XRD data. For the single-crystal refinement, we used a total of 5021 reflections, and all the reflections were well indexed by a monoclinic $\boldsymbol{a}_0 \times \boldsymbol{2b}_0 \times \boldsymbol{c}_0$ cell. We used $P112_1/a$ (no. 14) with a table setting choice: $c1$. No constraints were placed on the atomic positions. The comparison of calculated and observed intensity (F^2) after the structural refinement at room temperature is shown in Fig. 2a.

As regards the high-temperature (HT) phase, our single-crystal data could not uniquely solve the structure above T_c (HT-phase) due to the sizeable diffuse scattering. Most probably, at such high temperatures, lighter Na ions located in 1D tunnels of $NaRu_2O_4$ start to move within the tunnels. In this situation, we decided to begin with positional parameters of distorted phase (Table 2, LT-phase with $\boldsymbol{a}_0 \times \boldsymbol{2b}_0 \times \boldsymbol{c}_0$ $P112_1/a$ from Shelx refinement with twin), and generate undistorted positional parameters (undistorted $P112_1/a$ $\boldsymbol{a}_0 \times \boldsymbol{b}_0 \times \boldsymbol{c}_0$). The undistorted positional parameters of $P112_1/a$ symmetry are used to get positional parameters for orthorhombic HT-phase of *Pnma* symmetry under cell-symmetry and group-subgroup relation[19]. Expected coordinates at HT *Pnma* phase based on LT $P112_1/a$ structure ($\boldsymbol{a}_0 \times \boldsymbol{b}_0 \times \boldsymbol{c}_0$) are shown in Table 2. Excellent agreement is seen between expected positions and reported one[15] (by missing superlattice reflections: $\boldsymbol{a}_0 \times \boldsymbol{b}_0 \times \boldsymbol{c}_0$), as shown in Table 3.

The crystal structure of $NaRu_2O_4$ is close to that of the prototype compound $CaFe_2O_4$ with similar coordination environments. In our revised crystal structure for $NaRu_2O_4$, the most characteristic feature we found is the edge-sharing octahedra double RuO_6 chain, which runs along the crystallographic b-axis. These double chains form a two-leg zigzag ladder along the crystallographic b-axis. The RuO_6 octahedra are edge-sharing within each chain, tied to the neighboring chain through the corner oxygen. This leads to an interesting lattice geometry with pseudo-triangular tunnels, in which a single Na atom can be accommodated, as shown in Fig. 4a, which is also found in various $CaFe_2O_4$-type lattices[21–26]. Our detailed single-crystal x-ray diffraction analysis shows a transition from the HT (high-temperature) *Pnma* structure to the low-temperature (LT) $P112_1/a$ structure at $T_c = 535$ K, as shown in Fig. 4b, c: which is consistent with the results of resistivity measurements shown in Fig. 1a.

According to our diffraction experiments done between $300 \le T \le 575$ K, the $\mathbf{q} = (0, ½, 0)$ superlattice peak (satellite reflection) persist right up to 535 K as shown in Fig. 5. The line cut from the temperature-dependent reciprocal image analysis for peak $\mathbf{q} = (0, ½, 0)$ shows clearly the suppression of intensity as a function of temperature as in Fig. 5b, c. The $\mathbf{q} = (0, ½, 0)$ superlattice peak is substantially suppressed just above the first-order transition ($T_c = 535$ K).

Charge ordering and bond valence sum (BVS). The structure of $NaRu_2O_4$ can be visualized as the double chain of edge-sharing RuO_6 octahedra running in the b-direction and forming 2-leg zigzag ladders (see Fig. 6a). The corner-sharing oxygen atoms connect these ladders, also having a zigzag pattern. In effect, there appear in this system, not one, but *three* different types of zigzag ladders: those in edge-sharing double chains (ladders-2 marked by red in Fig. 6b. For shortness, we will call them "red" ladders), and two types of corner-sharing zigzag ladders, marked in Fig. 6b, c by blue and green. When describing this class of materials, one often pays primary attention to the phenomena occurring in the

Table 2 Expected coordinates at HT *Pnma* phase based on LT $P112_1/a$ structure ($a_0 \times b_0 \times c_0$) (atoms are at 4*c* site[19]).

Atoms	*x*	¼	*z*	$-x+1/2$	¾	$Z+1/2$	$-x$	¾	$-z$	$X+1/2$	¼	$-z+1/2$
Ru1	0.0580	0.25	0.1153	0.4420	0.75	0.6153	−0.0580	0.75	−0.1153	0.5580	0.25	0.3847
Ru2	0.0850	0.25	0.6026	0.4150	0.75	0.1026	−0.0850	0.75	−0.6026	0.5850	0.25	−0.1026
Na1	0.2395	0.25	0.3409	0.2605	0.75	−0.1591	−0.2395	0.75	−0.3409	0.7395	0.25	0.1591
O1	0.2950	0.25	0.6585	0.2050	0.75	0.1585	−0.2950	0.75	−0.6585	0.7950	0.25	−0.1585
O2	0.3849	0.25	0.9762	0.1151	0.75	0.4762	−0.3849	0.75	−0.9762	0.8849	0.25	−0.4762
O3	0.4730	0.25	0.2195	0.0270	0.75	−0.2805	−0.4730	0.75	−0.2195	0.9730	0.25	0.2805
O4	0.0863	0.25	0.9347	0.4137	0.75	0.4347	−0.0863	0.75	−0.9347	0.5863	0.25	−0.4347

Table 3 Reported LT *Pnma* structure ($a_0 \times b_0 \times c_0$) (atoms are at 4*c* site)[19].

Atoms	*x*	¼	*z*	$-x+1/2$	¾	$Z+1/2$	$-x$	¾	$-z$	$X+1/2$	¼	$-z+1/2$
Ru1	0.0603	0.25	0.1152	0.4397	0.75	0.6152	−0.0603	0.75	−0.1152	0.5603	0.25	0.3848
Ru2	0.0848	0.25	0.6036	0.4152	0.75	0.1036	−0.0848	0.75	−0.6036	0.5848	0.25	−0.1036
Na1	0.2399	0.25	0.3397	0.2601	0.75	−0.1603	−0.2399	0.75	−0.3397	0.7399	0.25	0.1603
O1	0.2946	0.25	0.6594	0.2054	0.75	0.1594	−0.2946	0.75	−0.6594	0.7946	0.25	−0.1594
O2	0.3847	0.25	0.9751	0.1153	0.75	0.4751	−0.3847	0.75	−0.9751	0.8847	0.25	−0.4751
O3	0.4730	0.25	0.2181	0.0270	0.75	−0.2819	−0.4730	0.75	−0.2181	0.9730	0.25	0.2819
O4	0.0870	0.25	0.9347	0.4130	0.75	0.4347	−0.0870	0.75	−0.9347	0.5870	0.25	−0.4347

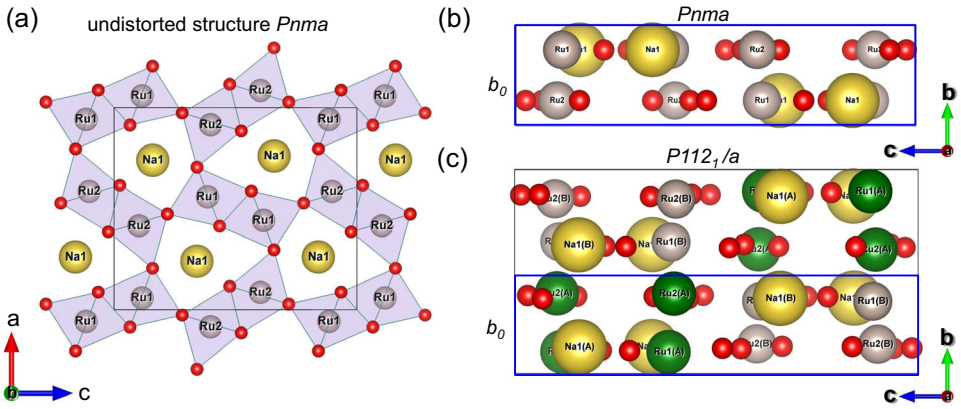

Fig. 4 High-temperature and low-temperature crystal structures. a The HT-phase in $NaRu_2O_4$ has an orthorhombic structure with a *Pnma* space group, similar to the $CaFe_2O_4$-type structure[1]. The octahedra and Ru atoms are represented in light brown and O atoms in red color. **b** The HT-phase crystal structure (*Pnma*) of $NaRu_2O_4$ in *bc*-plane. **c** The LT-phase crystal structure of $NaRu_2O_4$ has monoclinic symmetry $P112_1/a$.

"red" ladders (see ref. [27]). But the corner-sharing ladders are sometimes found to play a more critical role in systems like hollandite $K_2Cr_8O_{16}$[28]. As we will see below, these edge-sharing ladders also play a crucial role in $NaRu_2O_4$.

Here it is worthwhile to think about possibility of certain effect due to off-stoichiometry. In particular, one can ask whether the observed metallic behavior is related to a sample quality issue. For instance, it is known that such stoichiometry plays an important role in determining the low-temperature properties of RuP[29], whose high-quality powder samples exhibit a metal–insulator transition. On the other hand, single crystal of RuP, presumably off-stoichiometric, has a metallic ground state. For $NaRu_2O_4$, we can rule out this issue as our powder sample also shows a metallic behavior (see also Supplementary Fig. 2). Another point is that our heat capacity measurements taken on two different samples consistently show a finite gamma value at low temperature, which is consistent with the data reported in ref. [15].

An exciting picture now emerges from the detailed structural study. The HT-phase has two independent Ru sites (Ru_1 and Ru_2), equally spaced (2.82 Å) with the lattice constant b_0 along two Ru chains. The most prominent feature of the structural changes is the appearance of strong dimerization in Ru chains (legs of zigzag ladders), leading to cell-doubling in the *b*-direction (see Fig. 7a). Ru–Ru distance in short Ru dimers is 2.60 Å—even shorter than the Ru–Ru distance in Ru metal (2.65 Å). It is a clear sign of direct metal–metal bonding in such dimers—which quite unexpectedly coexist with metallic conductivity. Simultaneously with the dimerization in 1D Ru chains—legs of zigzag ladders, Ru sites themselves become inequivalent, Ru(A) and Ru(B), a clear sign of a site-centered charge ordering in $NaRu_2O_4$. The coexistence of bond- and site-centered orderings is extremely rare in metallic systems, making $NaRu_2O_4$ especially interesting.

Another essential feature of this superstructure is the difference of distances in the inter-chain bond length (interdimer), both in edge-sharing "red" and in corner-sharing "green" and "blue" ladders (Fig. 6b). The $Ru_1(A)$–$Ru_1(A)$ and $Ru_2(A)$–$Ru_2(A)$ distance in the edge-sharing ladder is 3.10 and 3.09 Å, while the $Ru_1(A)$–$Ru_1(B)$ and $Ru_2(A)$–$Ru_2(B)$ distance are 3.12 and 3.11 Å, respectively, with the remaining distance between dimers ($Ru_1(B)$–$Ru_1(B)$ and $Ru_2(B)$–$Ru_2(B)$) being 3.16 Å (see Fig. 7a, b). From the viewpoint of the bond order, short bonds have a shape like a "letter-Z" (see Fig. 8). The same is true for two other

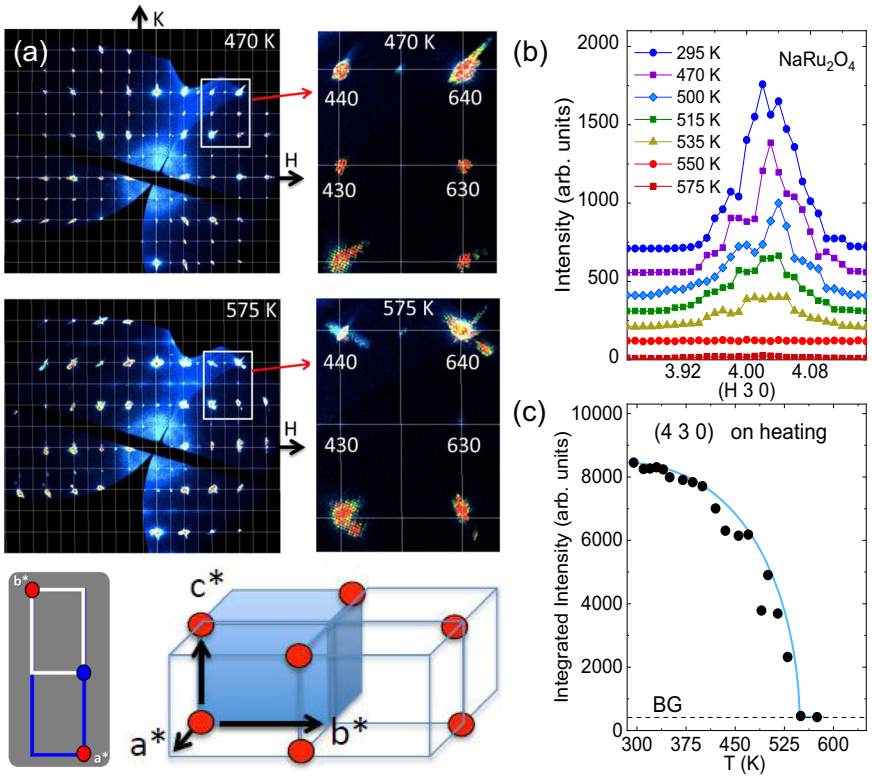

Fig. 5 Single-crystal x-ray diffraction (SC-XRD). a Reciprocal lattice maps of the SC-XRD data for $NaRu_2O_4$ obtained at 470 and 575 K with the first-order transition at $T_c = 535$ K. **b** The line cut for various temperatures below and above the first-order phase transition as extracted from the reciprocal space analysis. **c** Temperature dependence of the (4 3 0) super-lattice peak.

types of ladders, edge-sharing "blue" and "green" ladders. We thus see that the dimers also form *Z*-type orbital clusters in corner-sharing ladders. The relative difference of interdimer bonds in these is even more prominent than in the "red" edge-sharing ladders: it is ~1.7% compared to ~0.7% in the "red" ladders. This already hints that what happens in corner-sharing ladders is probably more critical than in edge-sharing ones, as in hollandite $K_2Cr_8O_{16}$[28]. According to our ab-initio calculations based on the charge valence of our choice [$Ru_1(A)^{3+}$, $Ru_1(B)^{4+}$, $Ru_2(B)^{4+}$, $Ru_2(A)^{3+}$), the nn hoppings in corner-sharing blue and green zigzags are: for blue corner-sharing bonds $t = 0.40$ eV, for green corner-sharing ones $t = 0.29$ eV, and for red edge-sharing bonds $t = 0.35$ eV. For other charge ordering the values are somewhat different but the blue corner-sharing bonds are always the strongest. It shows the dominance of the blue bond among all relevant bonds.

For the determination of the oxidation states of cations (Na and Ru), we carried out calculations by using the BVS method with an inbuilt program in Fullprof software[30]. The principle of BVS method in determining the valence V from different cation sites[31,32] can be given by an expression $V = \Sigma_i[\exp(d_0 - d_i)/0.37]$. Here, d_i is the experimental bond lengths to the surrounding ions, and d_0 is a tabulated empirical value characteristic for the cation-anion pair[31,32]. The BVS result for $NaRu_2O_4$ was determined for the LT-phase. The charge at different Ru sites is illustrated by different colors (brown-Ru^{4+} and green-Ru^{3+}) in Figs. 6 and 7. The BVSs for the eight oxygen sites were between 1.86 and 2.20. The BVSs for the four Ru cations sites for different charge configurations (we call them four different models) are shown below in Table 4. The respective reliability parameter as Global Instability Index (GII) is also listed for each BVS model for $NaRu_2O_4$.

To be more technical, an important question is how different Ru valence states are distributed in the low-temperature phase. Specifically, one has to know which ions, in which charge state, are connected by these shorter zigzag rungs in orbital *Z* clusters. For that, we used the results from the BVS analysis at each Ru, an empirical measure of its charge or its valence state[33,34]. In the HT-phase, all Ru are equivalent, and BVS gives the valence $Ru^{3.5+}$. In contrast, Ru ions in a short dimer are indeed inequivalent in the LT-phase, with the valence estimated from BVS being 3.536 and 3.106; that is, one can think of Ru^{4+} and Ru^{3+} in each dimer. However, from our structural data alone, although collected with high-resolution single-crystal x-ray diffraction and the total number of 5021 Bragg peaks, we cannot uniquely discriminate the four possible charge ordering patterns, mainly because an x-ray experiment fundamentally suffers from the weak scattering signals of oxygen. The reliability parameters (GII) for four different charge ordering patterns are comparable to one another, about 10–11% (see Table 4). Still, a slightly better index is obtained for charge distribution with Ru^{4+} ions at the ends of short diagonal bonds in blue and green ladders (reliability factor 10.43% for model 3 in Table 4). In contrast, these are Ru^{3+} in edge-sharing red ladders. Note that different ladders are connected in the structure of $NaRu_2O_4$ so that the charges at short zigzags in neighboring ladders are opposite (see Fig. 8).

Theoretical studies. As we commented above, there is unavoidable ambiguity about our determination of the charge valence using the BVS method although we used the total number of 5021 Bragg peaks from the high-resolution single-crystal x-ray diffraction experiment. Therefore we employed ab-initio LSDA and LSDA + U calculations to clarify the charge pattern favored by the LT crystal structure. We used different Coulomb repulsion U

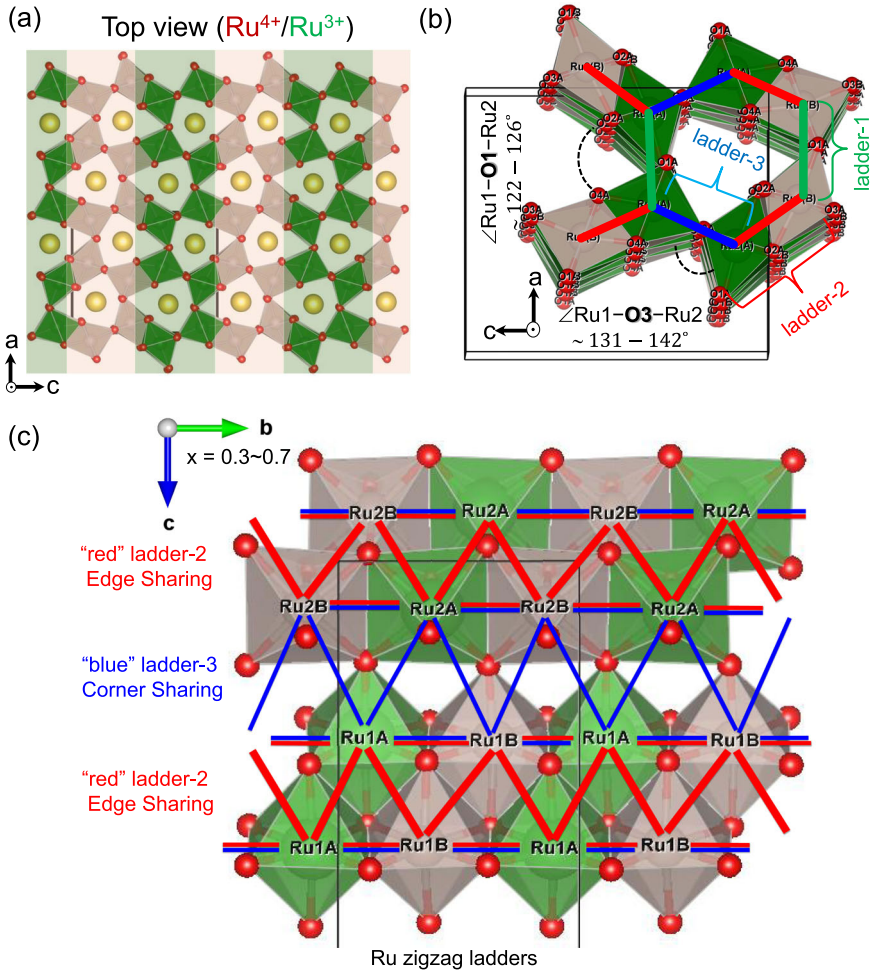

Fig. 6 Crystal structure of the tunnel compound $NaRu_2O_4$. a Top view of the low-temperature structure. **b** Illustration of different types of zigzag ladders: "red" ladders with edge-sharing RuO_6 octahedra; "green" and "blue" ladders with corner-sharing octahedra. **c** The detailed structure of corner-sharing and edge-sharing ladders.

values in the range 2.7–4.2 eV and Hund's coupling $J_H = 0.7$ eV as estimated from LSDA. All calculations were performed for the experimental HT and LT crystal structures. No attempts to optimize lattice geometry have been made. The effect of SOC on Ru t_{2g} bands was relatively weak. In the following, for simplicity, we discuss the results of scalar-relativistic calculations. Our theoretical studies show that different self-consistent spin and charge-ordered solutions can be stabilized for sufficiently large U (3.7 eV). These solutions have the following common features: Ru d_{xy} states (in local coordinates, with the axes directed from Ru to O) are strongly split into occupied bonding and unoccupied antibonding molecular orbital states (see Fig. 7c–f). Second, each dimer's Ru ions become formally Ru^{3+}, with its d_{xz}, d_{yz} orbitals being doubly occupied. Another Ru ion of the dimer, Ru^{4+}, has one half-occupied orbital, approximated by a linear combination of d_{xz} and d_{yz} lying in the plane perpendicular to the b-axis. The Ru^{4+} ion acquires a spin moment of about 0.8 μ_B. The orbital-resolved density of Ru d states illustrates the charge disproportionation. With decreasing U, the hybridization becomes more robust between the unoccupied d_{xz}, d_{yz} orbital of Ru^{4+} and occupied t_{2g} orbitals of Ru^{3+}, a gap separating the unoccupied d_{xz}, d_{yz} band from the top of the valence band closes, and for $U \sim 2.7$ eV the charge disproportionation between Ru^{3+} and Ru^{4+} ions disappears (see Fig. 7c–f). It should be noted that this is only a rough estimate for the critical U value which may change if optimized crystal structure were used in the calculations and is in general implementation specific.

Out of the four charge ordering patterns allowed for the LT structure, three are nearly degenerate, with the energy difference being <3 meV/f.u. This finding agrees with the BVS analysis results, which give comparable reliability factors for different charge ordering. Still, the lowest total energy is found for one charge ordering pattern: for which the lowest value of GII was obtained experimentally from BVS. The final charge pattern is that the short zigzag bonds in Z-cluster in corner-sharing "blue" ladders connect Ru^{4+} - Ru^{4+} ions (see Fig. 8).

Finally, we would like to note that the structure of $NaRu_2O_4$ is composed of frustrated 2-leg zigzag ladders with a spin-singlet ground state, which makes this material quite interesting. For more details see Supplementary Figs. 4 and 5 in Supplementary Note 4. As shown in Fig. 9a, b, the orthorhombic *Pnma* crystal structure of $NaRu_2O_4$ has two ruthenium atoms Ru_1 and Ru_2. The edge-sharing bond between the two RuO_6 octahedra for each dimer 1 (2.60 Å), dimer 2 (2.61 Å) and Z diagonal-bond (3.10 Å) give rise to two Ru–O–Ru bonds which are deviated from 90° for each and also all of the edge-sharing octahedral shows significant trigonal-distortion. The schematic representation shows the double chain-forming two-leg zigzag ladders (solid thick light-green, reddish-brown, and sky-blue lines) running along the crystallographic b-axis in crystal. The 2-leg zigzag ladders are

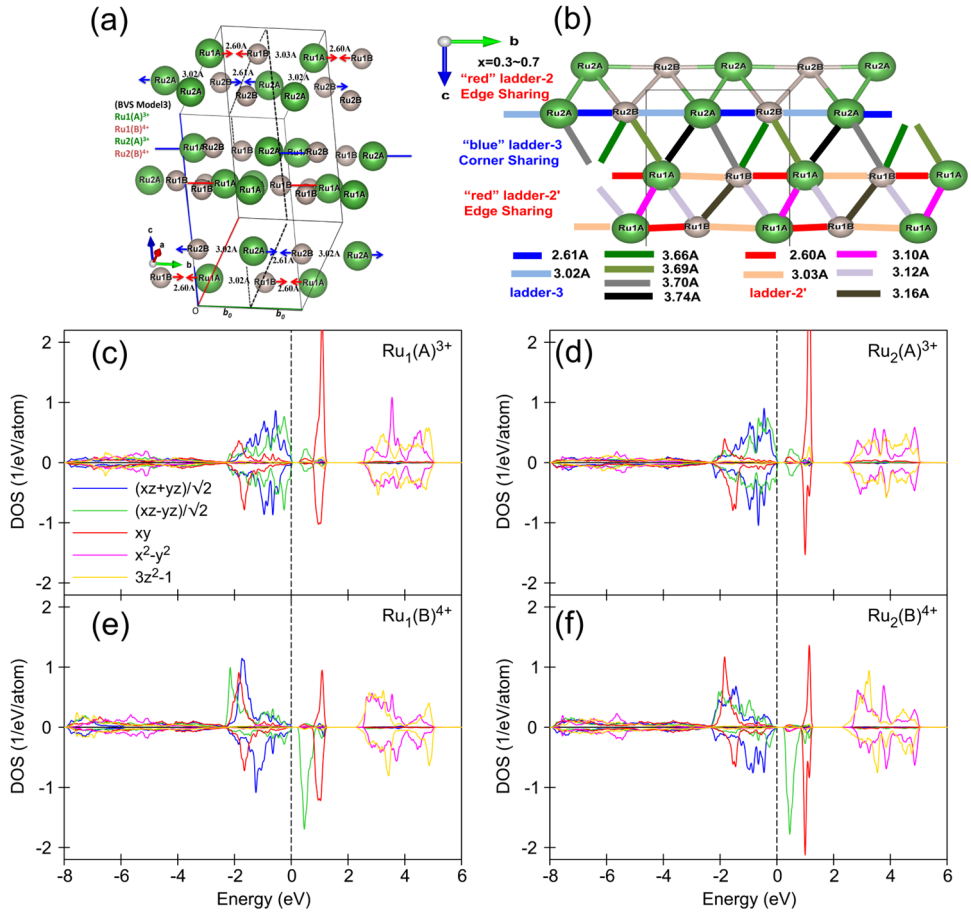

Fig. 7 Superstructure in the low-temperature phase and the results of the LSDA + *U* band structure calculations. a The unit-cell of the low-temperature phase with two dimerized Ru bonds and the valence of Ru as determined from bond valence sum (BVS) calculations. **b** Structure of the blue corner-sharing ladder with different valence states of Ru and different bond lengths marked. **c**–**f** Orbital-resolved DOS for four nonequivalent Ru atoms calculated within LSDA + U with $U = 3.7$ eV and $J = 0.7$ eV, assuming the charge order shown in (**a**). Ru orbitals are defined in local frames with the axes directed to the nearest O ions.

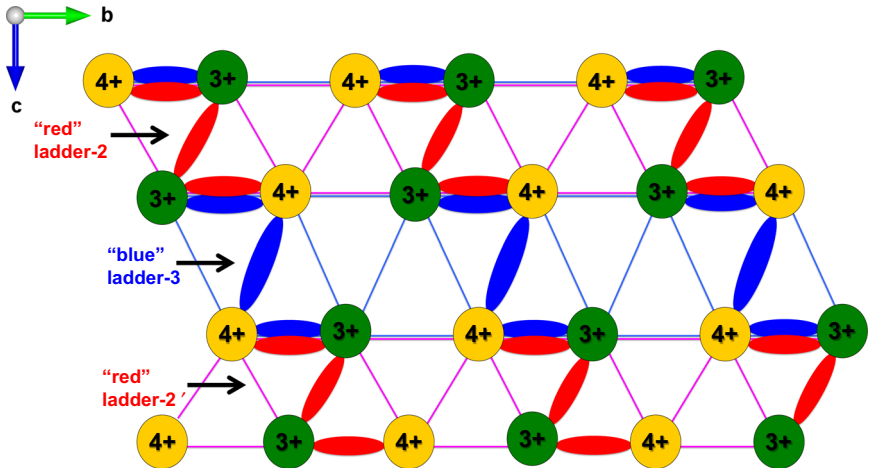

Fig. 8 *Z*-order in the two-leg corner- and edge-sharing RuO_6 zigzag ladders. The sketch of self-organized Z-clusters in the low-temperature phase, formed within the edge-sharing red and corner-sharing blue ladders of $NaRu_2O_4$ lattice in the low-temperature phase.

connected in two different forms: the corner- (blue or green ladders) or the edge- (red ladders) sharing RuO_6 octahedra. The t_{2g} energy-level sketch with respective electron fillings is shown for a charge-ordered state, so-called Z-order (left panel) and Ru-dimer (right panel) in Fig. 9d.

Conclusions

Thus the following final picture emerges from both the experimental and theoretical studies. $NaRu_2O_4$ has very strong dimerization below $T_c = 535$ K (in other words, strong metal–metal bonding with the use of xy-orbitals) in one-dimensional chains

Table 4 The four different models corresponding to four options for two dimers: counting from the left, (3+, 4+) in the upper dimer, (3+, 4+) in the lower dimer.

Atoms	Model-1			Model-2			Model-3			Model-4		
	Ass. val.	Res.	GII (%)	Ass. val.	Res.	GII (%)	Ass. val.	Res.	GII (%)	Ass. val.	Res.	GII (%)
Ru1(A)	4+	3.5+	10.56	3+	2.9+	10.85	3+	2.9+	10.43	4+	3.5+	11.02
Ru1(B)	3+	3.1+		4+	3.6+		4+	3.6+		3+	3.1+	
Ru2(A)	3+	2.9+		4+	3.5+		3+	2.9+		4+	3.5+	
Ru2(B)	4+	3.6+		3+	3.0+		4+	3.6+		3+	3.0+	

The summary of *Ru valences from the* bond-valence sum (BVS) calculations for different Ru sites in $NaRu_2O_4$ at 300 K shows different models below. The Model-3 looks consistent as per the observed dimerization on the two-leg zigzag ladder and our detailed LSDA + *U* calculations. Accordingly, we have used charges on the respective Ru sites in the $NaRu_2O_4$ crystal structure (Figs. 1 and 3a). The GII is the reliability parameter as Global Instability Index. The average valence on Ru sites is 3.5+.
Ass. Val. assumed valence, *Res.* results.

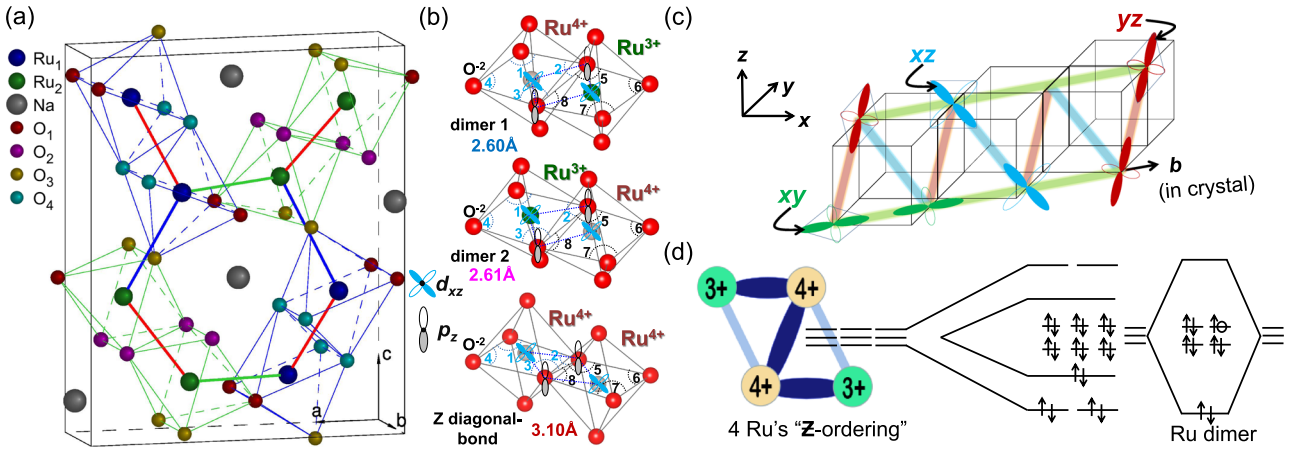

Fig. 9 $CaFe_2O_4$-type tunnel structure and edge-sharing RuO_6 two-leg ladders in $NaRu_2O_4$ lattice. a The orthorhombic *Pnma* crystal structure. **b** The bond between the two RuO_6 octahedra for each dimer 1 (2.60 Å), dimer 2 (2.61 Å), and *Z* diagonal-bond (3.10 Å). **c** Schematic representation of the double chain with two-leg zigzag ladders (solid thick light-green, reddish-brown, and sky-blue lines). **d** The two-leg zigzag ladders in two different forms, either corner- (blue or green ladders) or edge- (red ladders), sharing RuO_6 octahedra.

forming legs of zigzag ladders (this is a bond-centered CDW). With the average valence $Ru^{3.5+}$, one active electron (or one hole) remains per a dimer. And simultaneously with this dimerization (actually the orbitally driven Peierls dimerization[35–38]), these extra electrons order in each dimer—there appears also a site-centered charge ordering or site-centered CDW. The remaining electrons from one stronger diagonal bond between dimers in neighboring legs, creating *Z*-clusters (Fig. 8). The detailed form of orbitals in forming this short zigzag bond in the "blue" corner-sharing ladders is shown in Fig. 9c. But this extra bonding is not strong enough to make the system insulating, and it remains metallic below T_c due to the multi-orbital effect. These Ru–Ru dimers probably survive above T_c, forming dimer liquid as, e.g., in Li_2RuO_3[39]; this dimer liquid phase in Li_2RuO_3 was found stable upon doping too[40]. This could be checked by probes like EXAFS or PDF (pair distribution function) analysis.

To put our results in a broader perspective, we would like to comment on why the dimerization and the site-centered charge ordering coexistence are favorable for metallic $NaRu_2O_4$, while it has been rarely seen in other transition metal compounds: another example is $IrTe_2$[41]. Most importantly, the Ru 4*d* bands of $NaRu_2O_4$ exhibit the delicate balance between the correlations, the Coulomb *U*, and the bandwidth *W*. Two other factors play a crucial role: orbital freedom, leading to orbitally-driven dimerization, and the mixed-valence of Ru, $Ru^{3.5+}$, promoting site-centered charge ordering. These features seem to be the key to realizing charge ordering and dimer coexistence in a metallic $NaRu_2O_4$. Going further, we anticipate that our observations will prompt renewed efforts towards the hitherto scarcely investigated Mott–Hubbard physics in a metallic regime.

Methods

Sample preparations. Polycrystalline $NaRu_2O_4$ samples were synthesized by solid-state reaction of preheated RuO_2 (99.999%, Aldrich) and Na_2CO_3 (99.999%, Aldrich) under an Ar-gas environment at 950 °C for 90 h with several intermediate grindings and pelletization. Subsequently, high-quality single crystals of $NaRu_2O_4$ were grown from this polycrystalline powder via a modified self-flux vapor transport reaction under flowing Ar-gas (ultra-pure 99.999%). Long needle-shaped high-quality single crystals ($1 \times 0.1 \times 0.1$ mm^3) were obtained from the final products. The synthesized polycrystalline sample's phase purity was checked using a Bruker D8 Discover diffractometer with a Cu-Kα source with no impurity peaks observed. Elemental analysis was subsequently done confirming the samples' stoichiometry: we used a COXI EM-30 scanning electron microscope equipped with a Bruker QUANTAX 70 energy dispersive x-ray system.

Bulk properties. Electrical resistivity (ρ) measurements were carried out using a homemade system equipped with a furnace (300–685 K) and a pulsed-tube cryostat (down to 3 K, Oxford). The electrical resistance was measured in the four-point geometry on a static sample holder, where the contacts to the sample were made using silver paint and 25 μm gold wire. The current was applied perpendicular to the single crystal length, the crystallographic *b*-axis. Magnetic susceptibility $\chi(T)$ measurements were taken using an MPMS-SQUID magnetometer (Quantum Design). Heat capacity $C_p(T)$ measurements were made using the commercial Physical Property Measurement System (PPMS, Quantum Design).

Structure analysis. The temperature-dependent single-crystal x-ray diffraction (SC-XRD) was performed from 300 to 575 K using a single crystal diffractometer (XtaLAB P200, Rigaku). The room-temperature SC-XRD data exhibit super-structures $\mathbf{q} = (0, ½, 0)$. The crystal structure was refined by using Fullprof suite software and the *Shelx* program with a modified monoclinic merohedral twin

model under twin law as (-100) (010) (00-1) are presented in Supplementary Note 3. We also carried out temperature-dependent SC-XRD measurements on $NaRu_2O_4$ crystal to confirm the structural phase transition. Besides, we made a convergent beam electron diffraction (CBED) experiment, which is the most accurate in determining the correct symmetry of materials, especially regarding the loss of the inversion center. This CBED measurement allows us to determine the exact space-group of $NaRu_2O_4$. The CBED result for $NaRu_2O_4$ gives $P112_1/a$ symmetry and works well for the observed commensurate superstructures with $\mathbf{q} = (0, ½, 0)$.

LDA band calculations. Band structure calculations were performed for the experimentally obtained high- and low-temperature crystal structures using the LMTO method as implemented in the PY LMTO computer code[42] and the Perdew–Wang[43] parameterization of the exchange-correlation potential in the local spin density approximation (LSDA). To account for Coulomb repulsion within Ru d shell, we used a rotationally invariant formulation of the LSDA + U method[44] with the double-counting term in the fully localized limit. An LDA calculation for the HT crystal structure gave a nonmagnetic metallic solution with partially occupied Ru_1 and Ru_2 t_{2g} orbitals. The band structure's characteristic feature is Ru t_{2g} bands with stable quasi-one-dimensional dispersion along the b direction. These bands originate from Ru d_{xy} orbitals and are evidence of strong direct Ru d_{xy}–d_{xy} hopping along the b chains. Here and in the following, Ru orbital is defined in local frames with the axes directed approximately to three nearest O ions in such a way that the local [110] direction always points along the crystallographic b-axis. The LDA band structure calculated for the LT structure is qualitatively different. Although it remains nonmagnetic and metallic, the shortening of the Ru-Ru distance within dimers leads to the splitting of Ru d_{xy} drives bands into completely filled bonding states 2 eV below E_F and unoccupied antibonding ones 1 eV above E_F. The bonding d_{xy} bands accommodate one electron per Ru while the remaining 3.5 d electrons fill bands are formed by Ru d_{xz}, d_{yz} states.

Data availability

The relevant datasets generated and analyzed throughout this work are available from the corresponding authors upon reasonable request.

Received: 8 October 2021; Accepted: 3 January 2022;
Published online: 20 January 2022

References

1. Peierls, R. E. *Quantum Theory of Solids*. (Oxford University Press, 1955).
2. Wigner, E. On the interaction of electrons in metals. *Phys. Rev.* **46**, 1002–1011 (1934).
3. Lee, S. H. et al. Emergent excitations in a geometrically frustrated magnet. *Nature* **418**, 856–858 (2002).
4. Radaelli Paolo, G. et al. Formation of isomorphic Ir^{3+} and Ir^{4+} octamers and spin dimerization in the spinel $CuIr_2S_4$. *Nature* **416**, 155–158 (2002).
5. Lee, Seongsu et al. Spin gap in $Tl_2Ru_2O_7$ and possible formation of Haldane chains in three-dimensional crystals. *Nat. Mater.* **5**, 471–476 (2006).
6. Senn, M. S., Wright, J. P. & Attfield, J. P. Charge order and three-site distortions in the Verwey structure of magnetite. *Nature* **481**, 173 (2011).
7. Khomskii, D. I. *Transition Metal Compounds*. (Cambridge University Press, Cambridge, 2014).
8. Anderson, P. W. Resonating valence bonds: a new kind of insulator? *Mater. Res. Bull.* **8**, 153–160 (1973).
9. Ramirez, A. P. Geometric frustration: magic moments. *Nature* **421**, 483 (2003).
10. Balents, L. Spin liquids in frustrated magnets. *Nature* **464**, 199 (2010).
11. Savary, L. & Balents, L. Quantum spin liquids: a review. *Rep. Prog. Phys.* **80**, 016502 (2017).
12. Keimer, B. & Moore, J. E. The physics of quantum materials. *Nat. Phys.* **13**, 1045–1055 (2017).
13. Maeno, Y. et al. Superconductivity in a layered perovskite without copper. *Nature* **372**, 532–534 (1994).
14. Callaghan, A., Moeller, C. W. & Ward, R. Magnetic interactions in ternary ruthenium oxides. *Inorg. Chem.* **5**, 1572 (1966).
15. Regan, K. A., Huang, Q., Leec, M., Ramirez, A. P. & Cava, R. J. Structure and magnetism of $NaRu_2O_4$ and $Na_{2.7}Ru_4O_9$. *J. Solid State Chem.* **179**, 195 (2006).
16. Darriet, J. & Vidal, A. Les composés $NaRu_2O_4$ et $NaFeRuO_4$ structure cristalline de $NaFeRuO_4$. *Bull. Soc. Fr. Mineral. Cristallogr.* **98**, 374–377 (1975).
17. Yogi, A. et al. Symmetry breaking and unconventional charge ordering in single crystal $Na_{2.7}Ru_4O_9$. *Phys. Rev. B* **98**, 085113 (2018).
18. Tsuda, K. & Tanaka, M. Refinement of crystal structural parameters using two-dimensional energy-filtered CBED patterns. *Acta Crystallogr.* **A55**, 939–954 (1999).
19. *International Tables for Crystallography*, Vol. A (1983).
20. Sheldrick, G. M. A short history of SHELX. *Acta Crystallogr.* **A64**, 112–122 (2008).
21. Akimoto, J. et al. High-pressure synthesis and crystal structure analysis of $NaMn_2O_4$ with the calcium ferrite-type structure. *J. Solid State Chem.* **179**, 169–174 (2006).
22. Yamaura, K. et al. High-pressure synthesis, crystal structure determination, and a Ca substitution study of the metallic rhodium oxide $NaRh_2O_4$. *Chem. Mater.* **17**, 359 (2005).
23. Irifune, T., Naka, H., Sanehira, T., Inoue, T. & Funakoshi, K. In situ X-ray observations of phase transitions in $MgAl_2O_4$ spinel to 40 GPa using multianvil apparatus with sintered diamond anvils. *Phys. Chem. Miner.* **29**, 645 (2002).
24. Catti, M. High-pressure stability, structure and compressibility of Cmcm –$MgAl_2O_4$: an ab initio study. *Phys. Chem. Miner.* **28**, 729–736 (2001).
25. Irifune, T., Fujino, K. & Ohtani, E. A new high-pressure form of $MgAl_2O_4$. *Nature* **349**, 409 (1991).
26. Yamaura, K. et al. Spinel-to-$CaFe_2O_4$-type structural transformation in $LiMn_2O_4$ under high pressure. *J. Am. Chem. Soc.* **128**, 9448–9456 (2006).
27. Watanabe, T. et al. Orbital- and spin-driven instabilities in quasi-one-dimensional CaV_2O_4. *Phys. Rev. B* **98**, 094427 (2018).
28. Toriyama, T. et al. Peierls mechanism of the metal–insulator transition in ferromagnetic hollandite $K_2Cr_8O_{16}$. *Phys. Rev. Lett.* **107**, 266402 (2011).
29. Ootsuki, D. et al. Observation of metal to nonmagnetic insulator transition in polycrystalline RuP by photoemission spectroscopy. *Phys. Rev. B* **101**, 165113 (2020).
30. Rodriguez-Carvajal, J. Recent advances in magnetic structure determination by neutron powder diffraction. *Physica B: Condensed Matter* **192**, 55 (1993).
31. Brese, N. E. & O'Keeffe, M. Bond-valence parameters for solids. *Acta Crystallogr.* **B47**, 192 (1991).
32. Brown, I. D. *The Chemical Bond in Inorganic Chemistry: The Bond Valence Model*. (Oxford University Press, 2002).
33. Yamaura, K. et al. NaV_2O_4: a quasi-1D metallic antiferromagnet with half-metallic chains. *Phys. Rev. Lett.* **99**, 196601 (2007).
34. de Groot, J. et al. Charge order in $LuFe_2O_4$: an unlikely route to ferroelectricity. *Phys. Rev. Lett.* **108**, 187601 (2012).
35. Khomskii, D. I. & Mizokawa, T. Orbitally induced Peierls state in spinels. *Phys. Rev. Lett.* **94**, 156402 (2005).
36. Streltsov, S. V. & Khomskii, D. I. Covalent bonds against magnetism in transition metal compounds. *Proc. Natl Acad. Soc. USA* **113**, 10491 (2016).
37. Khomskii, D. I. & Streltsov, S. V. Orbital effects in solids: basics, recent progress, and opportunities. *Chem. Rev.* **121**, 2992–3030 (2021).
38. Bozin, E. S. et al. Local orbital degeneracy lifting as a precursor to an orbital-selective Peierls transition. *Nat. Commun.* **10**, 3638 (2019).
39. Kimber, S. A. J. et al. Valence bond liquid phase in the honeycomb lattice material Li_2RuO_3. *Phys. Rev. B* **89**, 081408(R) (2014).
40. Yun, S. et al. Doping effects on the valence bond solid of Li_2RuO_3 with Mn substitution. *Phys. Rev. B* **103**, 035151 (2021).
41. Pascut, G. L. et al. Dimerization-induced cross-layer quasi-two-dimensionality in metallic $IrTe_2$. *Phys. Rev. Lett.* **112**, 086402 (2014).
42. Antonov, V., Harmon, B. & Yaresko, A. *Electronic structure and Magneto-optical Properties of Solids*. (Kluwer Academic Publishers, 2004).
43. Perdew, J. P. & Wang, Y. Accurate and simple analytic representation of the electron–gas correlation energy. *Phys. Rev. B* **45**, 13244 (1992).
44. Yaresko, A. N., Antonov, V. N. & Fulde, P. Localized U 5*f* electrons in UPd_3 from LDA + U calculations. *Phys. Rev. B* **67**, 155103 (2003).

Acknowledgements

We would like to thank Juan Rodríguez-Carvajal, Sang-Wook Cheong, and Masahiko Isobe for fruitful discussions. Work at the Center for Quantum Materials was supported by the Leading Researcher Program of the National Research Foundation of Korea (Grant No. 2020R1A3B2079375) with partial funding by the Institute for Basic Science, Republic of Korea. The work of D. Kh. was supported by the Deutsche Forschungsgemeinschaft (DFG, German Research Foundation)—Project number 277146847—CRC 1238). A.K.Y. acknowledges financial support from the Institute for Basic Science of the Republic of Korea and was partially supported by the Research Fellowships of the Max-Planck Institute Foundation, Germany.

Author contributions

J.G.P. initiated and supervised the project. A.K.Y., H.S., and C.I.S. prepared the samples and carried out the bulk measurements. A.K.Y. did the structural analysis under the supervision of Y.N. D.M. and K.T. did the CBED measurements. J.N. did the merohedral-twin refinement by using Shelx software. A.Y. made the theoretical studies of LDA calculations. D.K. and J.-G.P. interpreted the data with the help of A.K.Y., A.Y., and Y.N. A.K.Y., A.Y., Y.N., D.K., and J.-G.P. wrote the manuscript with inputs from all authors.

Competing interests
The authors declare no competing interests.

Additional information
Supplementary information The online version contains supplementary material available at https://doi.org/10.1038/s43246-022-00224-8.

Correspondence and requests for materials should be addressed to Arvind Kumar Yogi or Je-Geun Park.

Peer review information *Communications Materials* thanks the anonymous reviewers for their contribution to the peer review of this work. Primary Handling Editor: John Plummer. Peer reviewer reports are available.

Reprints and permission information is available at http://www.nature.com/reprints

Publisher's note Springer Nature remains neutral with regard to jurisdictional claims in published maps and institutional affiliations.